Study of the Structural, Magnetic, and Electrical Properties of the 5H Hexagonal-Type Perovskite $BaMn_{0.2}Co_{0.8}O_{2.80}$

Laura Miranda,[†,‡] Antonio Feteira,[‡] Derek C. Sinclair,[‡] Mar García Hernández,[§] Khalid Boulahya,[†] María Hernando,[†] Aurea Varela,[†] Jose M. González-Calbet,[†] and Marina Parras*[,†]

Departamento de Química Inorgánica, Facultad de Químicas, Universidad Complutense de Madrid, E-28040 Madrid, Spain, Department of Engineering Materials, University of Sheffield, Mappin Street, Sheffield S1 3JD, United Kingdom, Instituto de Ciencia de Materiales de Madrid, CSIC, Cantoblanco, E-28049 Madrid, Spain

Received December 5, 2007. Revised Manuscript Received January 18, 2008

A combination of X-ray, neutron and electron diffraction, and high-resolution electron microscopy have been used to establish the 5H structural type of a new hexagonal-type perovskite $BaMn_{0.2}Co_{0.8}O_{2.80}$. The structure can be described as a (cc′chh) 5H hexagonal polytype with ordered oxygen vacancies where the cubic c′ layer corresponds to a composition of $[BaO_2]$ as opposed to $[BaO_3]$. The resulting layer structure consists of $[MnCo_2O_{12}]$ blocks of three sharing faces octahedra linked by corners to two unconnected $[CoO_4]$ tetrahedra. Electron Energy Switch order Loss Spectroscopy shows Mn to be present only as Mn(+IV) and therefore Co is present as mixed +III/+IV. Mn(+IV) and Co(+III) ions are distributed over the face sharing octahedral sites whereas Co(+IV) ions are located on the tetrahedral sites. The magnetic behavior is more complex than is observed for $BaCoO_{2.80}$ (a ferromagnet with T_c = 47 K) and can be described by a Stoner–Wohlfarth model of random-anisotropic, noninteracting monodomain ferromagnetic clusters. The ferromagnetic clusters occur below ~35 K and are assigned to groups of Co ions in octahedral and/or tetrahedral sites; however, incorporation of Mn ions in the octahedral sites disrupts the transition into long-range three-dimensional ferromagnetic order. Impedance Spectroscopy data reveals semiconducting grain conductivity at room temperature ($\sim 1 \times 10^{-2}$ S cm^{-1}); however, subambient data reveal an unusual temperature dependence with a smooth changeover from a thermally activated process (~0.07 eV) in the range 40–300 K to a low-temperature state below 40 K with a near-zero activation energy. The data cannot be described by conventional Arrhenius or variable-range hopping conduction models and the conduction mechanism(s) remain unresolved. Several possible suggestions for the conductivity behavior are made, including Anderson localization, anisotropic conduction associated with the 5H crystal structure or some complex correlated mechanism between the magnetic and electronic transport properties. The electrical microstructure of $BaMn_{0.2}Co_{0.8}O_{2.8}$ ceramics consist of semiconducting grains and constrictive grain boundaries and therefore exhibit internal barrier layer capacitor (IBLC) behavior, with a high and temperature-stable apparent permittivity of ~10 000 (at 10 kHz) above 100 K.

Introduction

Perovskite related AMO_3 mixed metal oxides are known to exhibit a diverse variety of useful electrical and/or magnetic properties, for example, ferroelectricity, ferromagnetism, ionic conduction, mixed conduction, superconductivity, and colossal magnetoresistance. In addition to possessing useful intrinsic (or bulk) properties, they can also be tailored to exhibit useful extrinsic properties. For example, inducing chemical heterogeneity (either by chemical doping and/or nonequilibrium cooling) in semiconducting perovskites, it is possible to develop resistive grain boundaries or outer surfaces on ceramics. Such electrical microstructures, consisting of semiconducting grains and insulating grain boundaries or surface layers, can give rise to extremely high apparent values of permittivity, commonly >10 000, that are temperature stable over a wide temperature range and they find applications as internal or surface barrier layer capacitors, respectively. Most commercial barrier layer capacitors are based on $(Ba,Sr)TiO_3$;[1] however, there has been considerable interest recently in a perovskite-related material $CaCu_3Ti_4O_{12}$.[2,3]

Many perovskites can be described as a close-packed arrangement of AO_3 layers with M cations occupying octahedral sites. Cubic stacking of the layers (ABC) occurs in many perovskites, e.g., $SrTiO_3$; this results in a three-dimensional array of corner-shared $[MO_6]$ octahedra and is commonly denoted as the 3C-type cubic perovskite (three-

* Corresponding author. E-mail: mparras@quim.ucm.es. Fax: (34) 91 394 43 52.
† Universidad Complutense de Madrid.
‡ University of Sheffield.
§ Instituto de Ciencia de Materiales de Madrid.

(1) Cheng, B. L.; Su, B.; Holmes, J. E.; Button, T. W.; Gabbay, M.; Fantozzi, G. *J. Electroceram.* **2002**, *9*, 17.
(2) Sinclair, D. C.; Adams, T. B.; Morrison, F. D.; West, A. R. *Appl. Phys. Lett.* **2002**, *80*, 2153.
(3) Adams, T. B.; Sinclair, D. C.; West, A. R. *Phys. Rev. B* **2006**, *73*, 094124.

10.1021/cm703447w CCC: $40.75
Published on Web 03/20/2008

layer cubic cell). Perovskites based exclusively on hexagonal close packing of AO_3 layers (AB) also occur and give rise to infinite chains of face-sharing octahedra arranged in a hexagonal net. This structure, denoted as the 2H-type (two-layer hexagonal cell) is adopted by $BaMnO_3$.[4] Between these 'extreme'-types of hexagonal and cubic perovskites, a wide variety of perovskite-based structures form by a combination of various cubic (c) and hexagonal (h) stacking layer sequences. As a result, many perovskite-type structures contain both corner- and face-sharing octahedra [MO_6]. Such materials are generally termed hexagonal polytypes and are denoted by the symbols nH or nR, where n represents the number of layers and H or R represent the symmetry (hexagonal or rhombohedral) of the unit cell.

Many factors such as cation size and oxygen content influence the crystal structure type of hexagonal perovskite-based materials. For example, the $BaMnO_{3-y}$ system[5–8] shows a rich variety of structural chemistry as a function of oxygen content such that reduction of the 2H-$BaMnO_3$ perovskite leads to different, stable hexagonal polytypes, i.e. 15R-, 8H-, 6H-, 10H- and 9R-type $BaMnO_{3-y}$.[9] In addition to anion content, the cation type and composition of both the A and M sublattices strongly influences the stabilization of a particular polytype. In particular, the size, electronic configuration and bonding preferences of the M-site cations commonly play a dominant role in the observed crystal chemistry of hexagonal perovskites. This can be illustrated by the large number of M-site doped $BaMnO_3$compounds with hexagonal perovskite-type structures that have been studied recently; among them, $BaMn_{1-x}In_xO_{3-y}$,[10] $BaMn_{1-x}Ti_xO_{3-y}$,[11] $BaMn_{1-x}Fe_xO_{3-y}$,[12–14] and $BaMn_{1-x}Co_xO_{3-y}$.[15–18] In addition to their structural diversity, some of these phases exhibit useful dielectric properties such as 12R-$BaMn_{0.5}Ti_{0.5}O_3$[11] and Mn-doped 6H-$BaTiO_3$.[19] Both systems exhibit high intrinsic permittivity values (>40) and resonate at microwave frequencies. The dielectric properties of these materials can be easily destroyed by inducing low levels of oxygen deficiency, either by heating in air at high temperatures or by annealing in inert or reducing atmospheres. The oxygen-deficiency induces mixed oxidation states of the M-site cations which results in semiconductivity due to electronic polaronic hopping on the M-site sublattice. For example, such behavior has been reported recently for 10H-$BaMn_{0.4}Fe_{0.6}O_{2.73}$.[14]

Recent investigation of the Ba−Mn−Co−O system has led us to establish the synthesis, crystal structure and magnetic (spin glass) behavior of the hexagonal cobaltite $BaMn_{0.4}Co_{0.6}O_{2.83}$.[18] The structure is closely related to the 12H $(cc'chhh)_2$ polytype with oxygen-deficient c′-BaO_2 layers whereby the oxygen distribution in the cubic layers leads to the formation of tetrahedral sheets. Here we report on the synthesis, crystal structure and physical properties of another phase in this system, $BaMn_{0.2}Co_{0.8}O_{3-y}$. Previous crystallographic studies on this compound have given conflicting results. For example, Gibb et al.[15] reported a 5H hexagonal polytype cell from Rietveld refinement of XRD data whereas Cherepanov et al.[17] proposed a 10H-type structure, although, in this case, only the unit-cell parameters were reported. To the best of our knowledge, the physical properties of this compound have not been reported.

To elucidate the crystal structure of $BaMn_{0.2}Co_{0.8}O_{3-y}$, a single-phase sample has been prepared and structural characterization has been performed using several techniques, including X-ray, neutron and selected area electron diffraction, electron microdiffraction, high-resolution electron microscopy, and electron energy loss spectroscopy (EELS). The magnetic and electrical properties have been investigated using ac and dc magnetic measurements and impedance spectroscopy, respectively, in an attempt to establish the structure–property relationships of the title compound.

Experimental Section

A polycrystalline sample of $BaMn_{0.2}Co_{0.8}O_{3-y}$ was prepared using the mixed oxide route from a well ground stoichiometric mixture of $BaCO_3$ (Aldrich, 99.98%), $MnCO_3$ (Aldrich, 99%) and Co_3O_4 (Aldrich, 100%) The mixture was decarbonated in a muffle furnace at 800 °C for 48 h, reground using an agate mortar and pestle, and then heated in a Pt crucible at 1000 °C for 2 days before being slow-cooled to room temperature at a cooling rate of a 4 °C/min. This process was repeated five times with intermediate grinding in an attempt to ensure sample homogeneity. Finally, the black powder was reground prior to heat treatment at 1050 °C for 48 h and then slow cooled to room temperature at a rate of 4 °C/min.

The average cation composition of the powder was determined by inductive coupling plasma (ICP), whereas the local composition was analyzed by energy-dispersive X-ray spectroscopy (EDS) with an INCA analyzer system attached to a JEOL 3000 FEG electron microscope. The overall oxygen content was determined by thermogravimetric analysis using a CAHN D-200 electrobalance, which allows the determination of variations of the oxygen content within $\pm 1 \times 10^{-3}$ on a sample of about 100 mg working under 500 mbar gas atmosphere. Experiments were performed by reduction under a 300 mbar H_2/200 mbar He atmosphere with a heating rate of 279 K/min up to a maximum temperature of 1123 K.

Powder X-ray diffraction (XRD) patterns were collected using Cu Kα monochromatic radiation (λ = 1.54056 Å) at room temperature on a Panalytical X'PERT PRO MPD diffractometer equipped with a germanium 111 primary beam monochromator and

(4) Hardy, A. *Acta Crystallogr.* **1962**, *15*, 179.
(5) Negas, T.; Roth, R. S. *J. Solid State Chem.* **1971**, *3*, 323.
(6) Parras, M.; González-Calbet, J. M.; Alonso, J.; Vallet-Regí, M. *J. Solid State Chem.* **1994**, *113*, 78.
(7) González-Calbet, J. M.; Parras, M.; Alonso, J.; Vallet-Regí, M. *J. Solid State Chem.* **1994**, *111*, 202.
(8) Parras, M.; Alonso, J.; González-Calbet, J. M.; Vallet-Regí, M. *J. Solid State Chem.* **1995**, 117.
(9) Adkin, J. J. A.; Hayward, M. A. *Chem. Mater.* **2007**, *19*, 755.
(10) Créon, N.; Michel, C.; Hervieu, M.; Maignan, A.; Raveau, B, *Solid State Sci.* **2003**, *5*, 243.
(11) Keith, G. M.; Kirk, C. A.; Sarma, K.; Alford, N. McN.; Cussen, E. J.; Rosseinsky, M. J.; Sinclair, D. C. *Chem. Mater.* **2004**, *16*, 2007.
(12) Caignaert, V.; Hervieu, M.; Domengès, B.; Nguyen, N.; Pannetier, J.; Raveau, B, *J. Solid State Chem.* **1988**, *73*, 107.
(13) Miranda, L.; Ramírez-Castellanos, J.; Hernando, M.; Varela, A.; González-Calbet, J. M.; Parras M, *Eur. J. Inorg. Chem.* **2007**, 2129.
(14) Miranda, L.; Boulahya, K.; Varela, A.; González-Calbet, J.; Parras, M.; Hernando, M.; Fernández-Díaz, M. T.; Feteira, A.; Sinclair, D. C. *Chem. Mater.* **2007**, *19*, 3425.
(15) Gibb, T. C. *J. Mater. Chem.* **1992**, *2* (4), 387.
(16) Taguchi, H.; Shimada, M.; Kanamaru, F.; Koizumi, M.; Takeda, Y. *J. Solid State Chem.* **1976**, *18*>, 299.
(17) Cherepanov, V. A.; Filonova, E. A.; Voronin, V. I.; Berger I. F, *J. Solid State Chem.* **2000**, *153*, 205.
(18) Miranda, L.; Ramírez-Castellanos, J.; Varela, A.; González-Calbet, J.; Parras, M.; Hernando, M.; Fernández-Díaz, M. T. *Chem. Mater.* **2007**, *19*, 1503.
(19) Keith, G. M.; Sarma, K.; Alford, N. McN.; Sinclair, D. C. *J. Electroceram.* **2004**, *13*, 305.

X'Celerator fast detector. Neutron powder diffraction (NPD) data were collected at room temperature and at 5 K on the high resolution powder diffractometer D1A at the Institute Laue Langevin (ILL), Grenoble, France, with neutrons of wavelength 1.908 Å. The angular range covered by the detectors extends from −10 to 160° with a step size of 0.05 °. Diffraction data were analyzed by the Rietveld method[20] using the Fullprof program.[21] The peak shape was represented by a Thompson-Cox-Hastings pseudo-Voigt function that includes a treatment of the axial divergence. According to this peak shape we have used a suitable formula described in the fullprofmanual for this peak shape to describe the angular dependence of the peak. *U*, *V*, *W*, *X*, and *Y* of the formula were parameters refined in the process. The 2θ zero point was refined and the background for each diffraction data point was also refined using a linear interpolation between 57 given points.

Selected area electron diffraction (SAED) and high-resolution electron microscopy (HREM) were performed using a JEOL 3000 FEG electron microscope, fitted with a double tilting goniometer stage (±22°, ± 22°). Simulated HREM images were calculated by the multislice method using the MacTempas software package.

EELS data were obtained from a Jeol 3000FEG TEM operating at 300 kV, equipped with Enfina EELS attachment. The energy resolution was better than 1 eV for all spectra as measured by the full-width at half-maximum (fwhm) of the corresponding zero-loss peak. Both the background and plural scattering have to be subtracted from the experimental spectra to isolate the white-line intensities. For convenience, the Hartree-Slater (HS) continuum model function (as directly provided by the EL/P program) was used for quantification.

DC magnetization was measured in a SQUID magnetometer, in the range ∼1.8 to 400 K under an applied magnetic field in the range 0−50 kOe. AC magnetic susceptibility was performed in a Quantum Design PPMS equipped with a magnet operating up to 90 kOe.

Powder was milled using a mortar and pestle and uniaxially pressed (Specac, Kent, U.K.) into cylindrical (length ∼5 mm) pellets under an applied pressure of 50 MPa and then isostatically pressed (model CIP 32330, Flow Autoclave System Inc., Columbus, OH) at 200 MPa. Pellets were sintered in air at 1323 K for 4 h and slow-cooled to room temperature at a rate of 4 °C/min, the same was done in the synthesis process, reaching a ceramic density of 5.59 g.cm^{-3} (70% of the theoretical X-ray density). Electrodes fabricated from gold paste (T-10112, Engelhard-CLAL, Cinderford, Gloucestershire, U.K.) were applied to both major faces of the pellets, which were sintered in air at 1073 K for 1 h to remove volatiles and harden the residue. The electrical properties of $BaMn_{0.2}Co_{0.8}O_{2.80}$ ceramics were investigated in the temperature range 10–300 K using a cryocooler coupled to an LCR bridge (model E4980A, Agilent, Palo Alto, CA) and to an impedance analyzer (model HP 4192A, Hewlett-Packard, Palo Alto, CA) for fixed frequency capacitance and Impedance Spectroscopy (IS) measurements, respectively. All impedance data were corrected for sample geometry and analyzed using the commercial software package Z-view (Scribner Associates, Inc., Charlottesville, VA, version 2.1).

Results and Discussion

The average cation composition established by a combination of ICP and energy dispersive X-ray analysis was in good agreement (within experimental errors) with the nominal starting composition. The oxygen content was determined by hydrogen reduction thermogravimetric analysis. BaO, MnO, and Co metal were identified by XRD as the final products of the reduction process. An observed weight-loss corresponding to 10.52% of the starting material, gave an overall composition for the powder to be $BaMn_{0.2}Co_{0.8}O_{2.80}$.

Structural Characterization. The XRD pattern (Figure 1a) can be indexed on the basis of a hexagonal unit cell with lattice parameters $a = 5.67225(5)$ Å and $c = 11.8813(1)$ Å; no impurity phase(s) were detected. The *c*-value corresponds to five layers per unit cell and therefore, on the basis of the XRD data, a 5H polytype as opposed to a 10H polytpe as reported previously by Cherepanov et al.[17] is stabilized for this composition. Nevertheless, structural characterization of the sample by SAED and HREM was undertaken to confirm the polytype.

Figure 2 a−c shows SAED patterns corresponding to $BaMn_{0.2}Co_{0.8}O_{2.80}$ along the most relevant zone axes, [010], [1$\bar{1}$0], and [001], respectively. The data are consistent with a 5H-polytype for which the only layer sequence is (ccchh), space group $P\bar{3}m1$.[22] According to this space group, all reflections are visible. No sign of disorder is observed by SAED. In fact, all diffraction spots appear sharp without any apparent streaking along the *c** axis. Figure 3 shows a [010] HREM image and simulation. In this zone, the structure is viewed parallel to the columns of Ba−O close packed rows and the stacking sequence of the layers is revealed directly. By consideration that Ba atoms are projected as brighter dots, the experimental contrast is associated with a (ccchh) layered sequence (see figure). This sequence extends through the whole crystal, therefore the presence of any significant intergrowths with other polytypes can be discounted. An image calculated with the ideal atomic positions corresponding to a (ccchh)-5H polytype (see inset in Figure 3) fits well with the experimental image for $\Delta t = 5$ nm, $\Delta f = 82.5$ nm.

A combined structural refinement of XRD and ND data was performed using the structural parameters of (cc′chh) 5H-$BaCoO_{2.8}$ polytype as a starting model.[23] This structure is closely related to the ideal 5H polytype with oxygen-deficient cubic c′-BaO_2 layers. This framework forms a laminar structure formed by two layers of unconnected tetrahedra linked by corners to the trimers of face-sharing octahedra. It is noteworthy that ND data were particularly useful in elucidating the distribution of Co and Mn over the different oxygen polyhedra due their different neutron scattering lengths, i.e., 2.49 and −3.75 fm, respectively.

Although most layered perovskites are hexagonal, the presence of oxygen-deficient BaO_2 layers can create a change in symmetry from hexagonal to orthorhombic due to displacement of the Ba and O atoms from the hexagonal special positions. This is the case for 10H-$BaFeO_{2.80}$ which forms crystals with the orthorhombic *Cmcm* space group. This subtle orthorhombic distortion does not introduce significant differences in powder XRD patterns, and according to Delattre et al.,[24] it seems possible that in some cases,

(20) Rietveld, H. M. *J. Appl. Crystallogr.* **1969**, *2*, 65.
(21) Rodríguez-Carvajal, *J. Phys. B* **1993**, *192*, 55.
(22) *International Tables for X-Ray Crystallography*; International Union for Crystallography: Chester, U.K., 1959; Vol. II: Mathematical Tables. p 342.
(23) Boulahya, K.; Parras, M.; González-Calbet, J.; Amador, U.; Martínez, J. L.; Tissen, V.; Fernández-Díaz M.T, *Phys. Rev. B* **2005**, *71*, 144402.

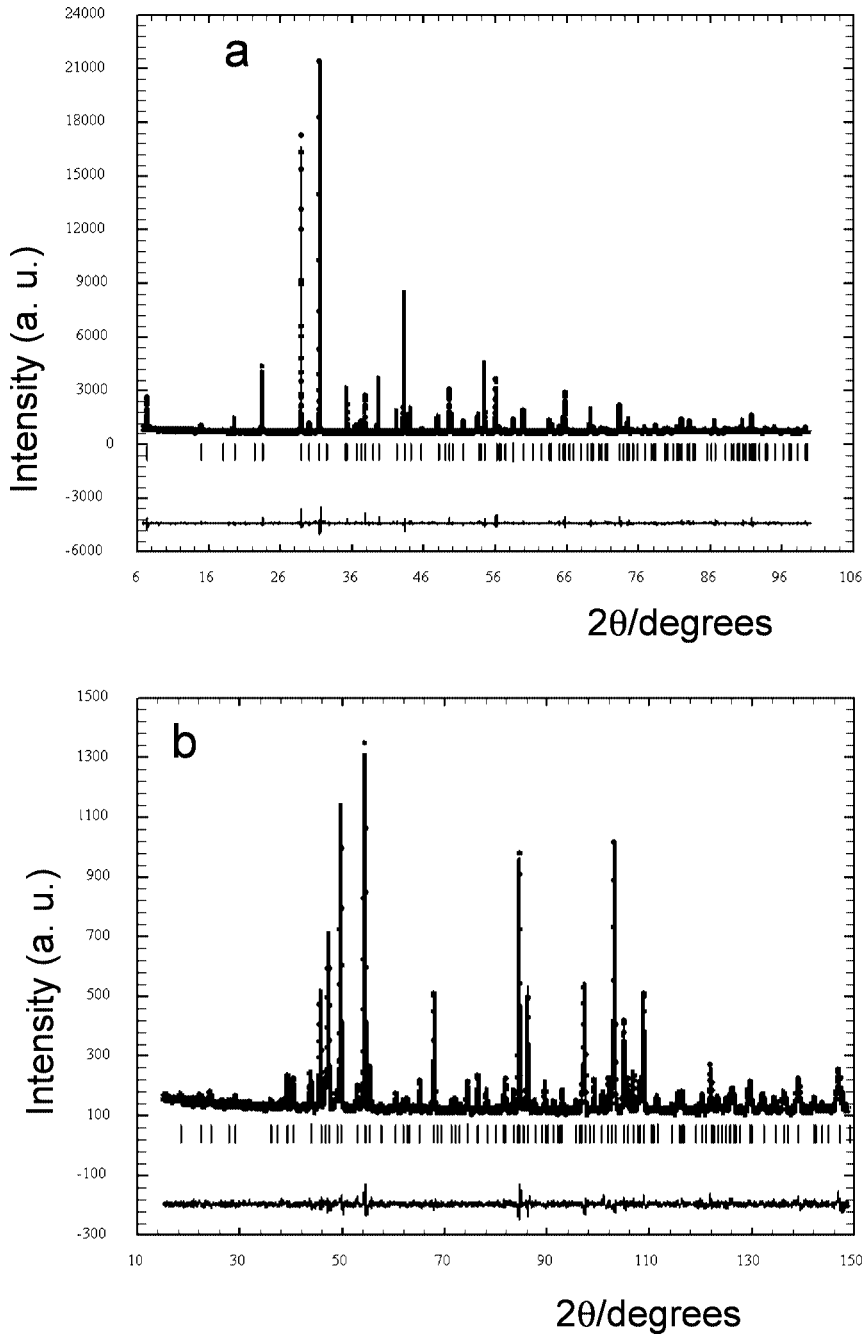

Figure 1. Observed, calculated, and difference profile of (a) X-ray and (b) neutron diffraction patterns for $BaMn_{0.2}Co_{0.8}O_{2.80}$ at room temperature.

such distortions can be modeled as hexagonal disorder. To ensure the correct symmetry of $BaMn_{0.2}Co_{0.8}O_{2.80}$ was obtained an electron microdiffraction study was performed. An electron microdiffraction pattern along [001] is shown in Figure 2d. Only diffraction maxima corresponding to a basic hexagonal cell are observed (unit cell is depicted); six mirror planes are observed and superimposed in the figure, suggesting *P6mm* symmetry. This result confirms the hexagonal symmetry of the crystal and whole pattern (zolz + holz) symmetry of *P6mm*.[25] A structural refinement based on 5H-$BaCoO_{2.80}$ in the $P\bar{3}m1$ space group[23] was therefore confirmed as an appropriate starting model.

Initially, Mn and Co were randomly distributed over the three available M sites (two octahedral and one tetrahedral) and the total metal occupancies were refined. The occupancies refined to unity within error and were fixed at this value. Subsequently, the ratio of each metal (Co/Mn) over the different polyhedra was allowed to vary, subject to the overall stoichiometry remaining constant. The atomic position and isotropic displacement parameters were refined independently for each atom except for O1 where anisotropic displacement parameters were refined. Refinements of the oxygen site occupancies did not reveal vacancies in the anion sublattice (for a composition of $O_{2.80}$), in agreement with the TGA results.

The structural parameters for 5H-$BaMn_{0.2}Co_{0.8}O_{2.80}$ resulting from the Rietveld refinement of powder XRD and ND data are listed in Table 1 and selected interatomic distances and angles are given in Table 2. The observed, calculated and difference profiles for both XRD and ND data are shown

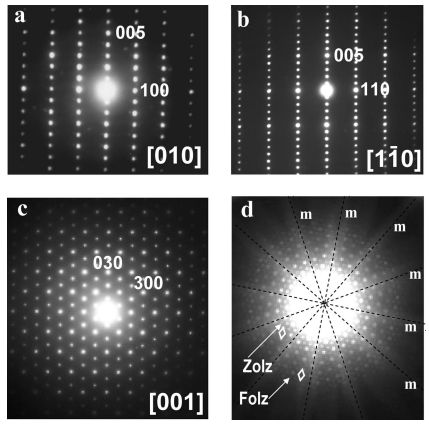

Figure 2. (a−c) SAED patterns along zone axes [010], [110], and [001], respectively, and (d) microdiffraction pattern along [001] for $BaMn_{0.2}Co_{0.8}O_{2.80}$.

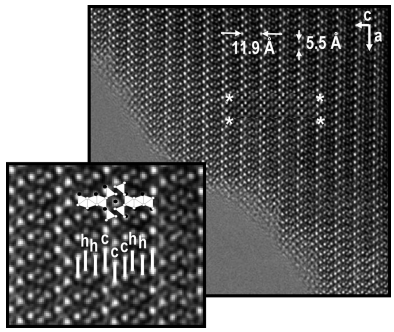

Figure 3. [010] HREM image and simulation for $BaMn_{0.2}Co_{0.8}O_{2.80}$.

in panels a and b in Figure 1, respectively. A good fit between calculated and experimental data was achieved as highlighted by the low *R*-values. It should be noted that no magnetic reflections were detected in the ND data collected at 5 K.

A schematic representation of the structure is depicted in Figure 4. A layered structure is formed by strings of three face-sharing octahedra linked by corners to a double layer of tetrahedra. The replacement of 20% Co by Mn in $BaCoO_{2.8}$ does not modify the essential structural features of the cobalt phase and therefore $BaMn_{0.2}Co_{0.8}O_{2.80}$ is isostructural with $BaCoO_{2.8}$.[23] The distribution of Mn and Co over the different polyhedra is summarized in Table 1. The tetrahedral sites (M3) are fully occupied by Co whereas Mn and Co are randomly distributed over the two crystallographically distinct sites in the octahedral trimers. The refinement of the cation site occupancies reflects the tendency for Mn to prefer face-sharing octahedral sites. Such a tendency has also been observed for 12H-$BaMn_{0.4}Co_{0.6}O_{2.83}$;[18] however, Mn is located mainly in the central positions of the face sharing octahedral tetramers for the 12H compound whereas in the present case of the 5H compound there is an almost equally distribution of Mn in the outer and central octahedra of the trimers.

The central octahedron of the trimer is not completely regular since although the six M1−O distances are identical (1.901 Å), the O3−M1−O3 angles (see Table 2) deviate somewhat from the ideal octahedral values (90 °). The M1−O distances are in excellent agreement with that observed for Co−O in the same environment: 1.874 Å in 2H-$BaCoO_3$,[26] 1.896 Å in 5H-$BaCoO_{2.80}$,[23] and 1.91 Å in 12H-$BaCoO_{2.6}$.[27] This observation is in agreement with the major occupation of Co in this site. The terminal octahedron is distorted with different M2−O2 and M2−O3 distances due to displacement of the metal atoms from the center toward the oxygen atoms in the cubic layer, i.e., to the neighboring tetrahedral sharing corner. Such a displacement is rather common in these polytypes since it reduces electrostatic repulsion between cations in adjacent face-sharing octahedra. For instance, this behavior has also been observed in 12H-$BaMn_{0.4}Co_{0.6}O_{2.83}$[18] and 12R-$BaMn_{0.5}Ti_{0.5}O_3$.[11] The M2−O distances are very similar to (Co, Mn)−O distances in the outer octahedral environment in 5H-$Ba_5Co_5O_{14}$ (1.94, 1.90 Å),[23] 12H-$BaCoO_{2.6}$ (1.978, 1.980 Å),[27] and 12H-$BaMn_{0.4}Co_{0.6}O_{2.83}$ (1.90, 1.96 Å).[18] As in 5H-$BaCoO_{2.80}$ or 12H-$BaMn_{0.4}Co_{0.6}O_{2.83}$, the shortest M−O distance in the structure corresponds to Co−O1, i.e., the only nonshared oxygen.

The thermal factors for Ba1 and O1, that constitute the non close packed oxygen-deficient BaO_2 layer, reflect the presence of disorder, thus, the corresponding anisotropic displacement parameters were refined; see ellipsoids in Figure 4. The high values for O1 in the xy plane are indicative of delocalization of this atom around its mean position. These static displacements are not ordered through the structure, then no reduction in crystal symmetry is necessary and the trigonal symmetry is preserved although such disorder is reflected in the corresponding thermal parameters. This feature has also been observed in other compounds with considerable anion disorder, for instance in the brownmillerite $Ba_2In_2O_5$[28] and in other hexagonal perovskites such as 5H-$BaIr_{0.2}Co_{0.8}O_{2.83}$,[29] 10H-$BaMn_{0.4}Fe_{0.6}O_{2.73}$,[14] and $Ba_5Er_2Al_2ZrO_{13}$.[30]

The refined composition $BaMn_{0.18(2)}Co_{0.82(2)}O_{2.80}$ is consistent both with the nominal composition and that obtained by the chemical analysis/TGA results. Charge neutrality for an oxygen content of 2.8 requires an average charge of 3.6+/cation in the M sublattice which corresponds to 0.4 M^{3+}/0.6 M^{4+} per formula unit. To establish the formal oxidation state of Mn in $BaMn_{0.20}Co_{0.8}O_{2.8}$, an EELS study was performed using $BaMnO_3$[4] (Mn^{4+}) and $TbMnO_3$[31] (Mn^{3+}) compounds as internal standards. The Mn L2,3 edges for $BaMnO_3$, $BaMn_{0.20}Co_{0.8}O_{2.8}$ and $TbMnO_3$, normalized to the intensity of the L3 maximum, are shown in Figure 5. The results show the Mn oxidation state in $BaMn_{0.2}Co_{0.8}O_{2.8}$ to be similar to that of the $BaMnO_3$ internal standard; significant differences are observed on comparison with the spectrum for $TbMnO_3$. Analysis of MnL2,3 edge positions, the energy difference of the Mn(L2-L3) edges and the intensity ratio of the Mn(L3/L2) edges all indicate Mn to be in the +4

(24) Delattre, J. D.; Stacy, A. M.; Siegrist T, *J. Solid State Chem.* **2004**, *177*, 928.
(25) Morniroli, J. P.; Steeds J.W, *Ultramicroscopy* **1992**, *45*, 219.
(26) Taguchi, H.; Takeda, Y.; Kanamaru, F.; Shimada, M.; Koizumi, M. *Acta. Crystallogr., Sect. B* **1977**, *33*, 1298.
(27) Jacobson, A. J.; Hutchison, J. L. *J. Solid State Chem.* **1980**, *35*, 334.
(28) Berastegui, P.; Hull, S.; García-García, F. J.; Eriksson S.-G, *J. Solid State Chem.* **2002**, *164*, 119–130.
(29) Vente, S. J.; Battle P.D, *J. Solid State Chem.* **2000**, *152*, 361–373.
(30) Shpanchenko, R. V.; Abakumov, A.; Antipov, E. V. *J. Solid State Chem.* **1995**, *118*, 180.
(31) Kimura, T.; Goto, T.; Shintani, H.; Ishizaka, K.; Arima, T.; Tokura Y, *Nature* **2003**, *426*, 55.

Table 1. Structural Parameters from the Refinement for 5H-$BaMn0_{.2}Co_{0.8}O_{2.8}$[a]

atom	site	*x*	*y*	*z*	*B* (Å^2)	occ
Ba1	1a	0	0	0	1.1(1)	1
Ba2	2d	1/3	2/3	0.7721(3)	0.26(6)	1
Ba3	2d	1/3	2/3	0.4173(3)	0.28(7)	1
M1	1b	0	0	0.5	0.6(2)	0.74(2)/0.26(2)[b]
M2	2c	0	0	0.2912(5)	0.4(2)	0.67(2)/0.33(2)[b]
M3	2d	1/3	2/3	0.1394(5)	1.1(2)	1/0[b]
O1	2d	1/3	2/3	−0.0088(7)	[c]	1
O2	6i	0.1610(4)	0.8390(4)	0.1978(3)	1.02(8)	1
O3	6i	0.1482(3)	0.8518(3)	0.6026(4)	0.56(7)	1

[a] Space group $P\bar{3}m1$ (164), $a = 5.67225(5)$ Å, $c = 11.88133(16)$ Å. Fit parameters for neutron diffraction data: $R_F = 3.79$, $R_{wp} = 4.85$, $R_{exp} = 4.0$, $R_B = 3.42$, $\chi^2 = 1.49$. For X-ray diffraction data: $R_F = 3.18$, $R_{wp} = 4.34$, $R_{exp} = 3.60$, $R_B = 4.58$, $\chi^2 = 1.46$. [b] Co/Mn. [c] O1: β_{11}= 0.064(5), β_{22}= 0.064(5), β_{33}=0.0019(6), β_{12}=0.032(3), β_{13}=0, β_{23}=0

Table 2. Selected Interatomics Distances (Å) and Angles (deg) in 5H-$BaMn_{0.2}Co_{0.8}O_{2.83}$

Ba1−O1	3.2794(3)×6	M1−M2	2.483(6) ×2	O3−M1−O3	83.2(2)
Ba1−O2	2.836(4) ×6	M2−M3	3.745(4)	O3−M1−O3	180.0(3)
				O3−M1−O3	96.8(3)
Ba2−O1	2.604(8) ×3	M1−O3	1.901(3) ×6		
Ba2−O2	2.862(2) ×6			O2−M2−O2	90.2(2)
Ba2−O3	2.716(5) ×3	M2−O2	1.934(5) ×3	O2−M2−O3	93.8(3)
		M2−O3	1.928(5) ×3	O2−M2−O3	174.1(3)
Ba3−O2	3.113(4) ×3			O3−M2−O3	81.8(1)
Ba3−O3	2.868(4) ×3	M3−O1	1.76(1)		
Ba3−O3	2.854(2) ×6	M3−O2	1.832(4) ×3	O1−M3−O2	112.3(5)
				O2−M3−O2	106.5(2)

state in $BaMn_{0.20}Co_{0.8}O_{2.8}$. To ensure electroneutrality, the formal oxidation state for cobalt is therefore +3.5. By considering that Co^{3+} is strongly stabilized in octahedral coordination as well as the smaller size of Co^{4+}, the tetrahedral sites are preferentially occupied by Co^{IV}; the octahedral sites are occupied by Co(III) and Mn (IV) giving rise to the following formula: $Ba(Co^{4+}{}_{0.4})_{Td}$ $[(Co^{3+}{}_{0.27}Mn^{4+}{}_{0.13})_{M2}$ $(Co^{3+}{}_{0.14}Mn^{4+}{}_{0.05})_{M1}]_{Oh}O_{2.80}$.

The above results show that $BaMn_{0.2}Co_{0.8}O_{2.80}$ adopts a (cc′chh)-5H polytype structure. Such a polytype is not observed in the $BaMnO_{3-y}$[9] system for any anion stoichiometry; however, it is adopted for $BaCoO_{2.80}$.[23] In fact, in all hexagonal cobaltites reported to date, the presence of anion vacancies stabilizes structures containing a cc′c structural unit where c′ refers to a cubic BaO_2 layer. This results in the formation of a double tetrahedral layer. This tetrahedral oxygen coordination is likely for Co^{4+} and this seems to have a "structure-directing" effect on the stacking sequences adopted. With the exception of the 5H-type, the $(cc'chhh)_2$-12H polytype is the only structure adopted by oxygen-deficient hexagonal cobaltites. $BaCoO_{2.6}$,[27] $Ba_{0.9}CoO_{2.6}$,[32] and $BaCo_{0.4}Mn_{0.6}O_{2.83}$[18] all crystallize with this structure in which two layers of unconnected tetrahedra are linked by sharing corners to strings of four face sharing octahedra. Both polytypes, 5H and 12H, therefore, incorporate the cc′c stacking repeat to accommodate anion vacancies. Such behavior is in contrast to that reported for $BaMnO_{3-y}$[9] where anion vacancies in the oxygen-stoichiometric 2H-$BaMnO_3$ (hhh) stabilizes different polytypes which also incorporate cubic layers but with the anion vacancies located in h- rather than c-stacked layers.

According to Adkin et al.,[9] this preferential location for oxygen-deficiency in h-stacked layers for the $BaMnO_{3-y}$ system can be rationalized by examining the different coordination environments adopted by oxide ions in the structures, particularly the barium−oxygen bonds. The calculated averaged distances reveal that oxide ions within c-stacked layers have the shortest distances indicating the strongest bonding interaction. Removal of these oxide ions would result in the largest loss of lattice energy and, consequently, anion vacancies are located in the h-stacked layers. In a similar way, we have examined the influence of the Ba−O interactions in the location of anion vacancies in these hexagonal-type cobaltites. In the case of the 5H-type, there are three different environments for the oxide ions (Figure 4): The central layer of an hhc (A), an hcc' (B) or an cc'c (C) stack. The calculated Ba−O distances (Table 3) for each site shows that oxide ions in the central cubic layer in the ccc block have the longest bonds, and therefore, the weakest interaction. To remove these oxide ions seems to be the most favorable process. This may be a general feature for all anion-deficient hexagonal-type cobalt oxides.

Magnetic Properties. Magnetic susceptibilty data for $BaMn_{0.2}Co_{0.8}O_{2.80}$ measured in zero field cooling (ZFC) and

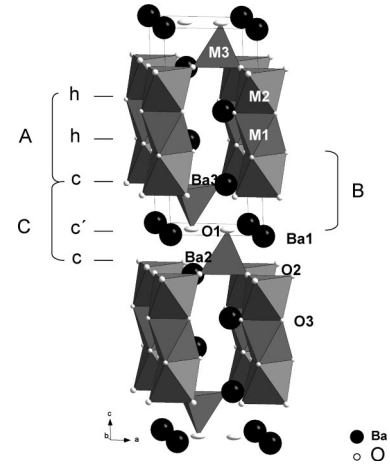

Figure 4. Structural Model for 5H-$BaMn_{0.2}Co_{0.8}O_{2.80}$.

(32) Maignan, A.; Hèrbert, S.; Pelloquin, D.; Pralong V, *J. Solid State Chem.* **2006**, *179*, 1852.

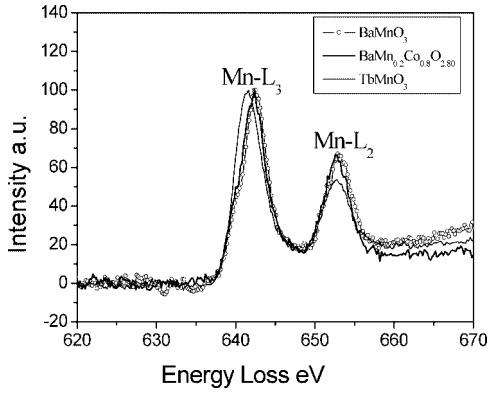

Figure 5. EELS spectra of the Mn L2,3 edges for $BaMnO_3$, $BaMn_{0.2}Co_{0.8}O_{2.80}$, and $TbMnO_3$. Data have been normalized to the intensity of the L3 maximum.

Table 3. Barium−oxygen Bond Lengths for the Different Anion Locations

anion site	bond	distance (Å)
hhc (A)	Ba in	2.854
	Ba out_h	2.868
	Ba out_c	2.716
	average	2.823
hcc′ (B)	Ba in	2.862
	Ba out_h	3.113
	Ba $out_{c'}$	2.836
	average	2.918
cc′c (C)	Ba in	3.279
	Ba out_c	2.604
	Ba out_c	2.604
	average	2.942

in a 1 kOe field on cooling (FC) is shown in Figure 6. Two major features are apparent. First, the magnetization increases sharply below 45 K and, second, a large irreversibility develops between the ZFC and FC data below 20 K. The general form of the data is compatible with that of a glassy system but is not exclusive to these materials, since random anisotropic ferromagnets and superparamagnets can also present similar features.[33] Indeed, the non saturation behavior of the FC data below the peak where the irreversibility develops may be better ascribed to a random anisotropic system. No magnetic reflections were revealed in the low temperature (5 K) neutron diffraction data, so no long-range order is expected for $BaMn_{0.2}Co_{0.8}O_{2.80}$. A Curie–Weiss analysis of the inverse of the magnetic susceptibility vs temperature data from 200 to 300 K renders a paramagnetic moment of 3.7 μ_B/metal ion and a Weiss constant $\Theta \approx 59$ K indicating predominantly ferromagnetic character of the magnetic interactions in the system, as observed for $BaCo_{0.6}Mn_{0.4}O_{2.83}$[18] and $BaCoO_{2.8}$.[23] In fact, $BaCo_{0.8}Mn_{0.2}O_{2.80}$ exhibits intermediate magnetic behavior between them; $BaCo_{0.6}Mn_{0.4}O_{2.83}$ is a spin glass whereas $BaCoO_{2.8}$ is a ferromagnet with $T_c = 47$ K.

An effective moment for $BaMn_{0.2}Co_{0.8}O_{2.8}$ was calculated on the basis of the crystallochemical assumption described above, namely, Co^{IV} in tetrahedral coordination and Mn^{IV} and Co^{III} randomly distributed in octahedral sites. In Ba_2CoO_4,[34,35] Co^{4+} is tetrahedrally coordinated and is in a

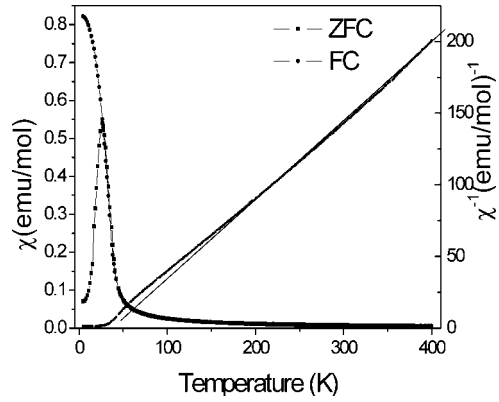

Figure 6. ZFC and 1 kOe FC magnetic susceptibility data for $BaMn_{0.2}Co_{0.8}O_{2.80}$. A Curie–Weiss plot of the magnetic susceptibility data is also included as well as its corresponding fit.

high spin configuration (5.91 μ_B). Assuming a low spin electronic configuration for Co^{III} (0 μ_B) and a Co^{4+}:Co^{3+} = 1:1 ratio, gives a calculated paramagnetic moment of 4.11 μ_B/metal ion. Although this value agrees well with the experimental one, it is worth noting that in the isostructural 5H-$BaCoO_{2.8}$, or in other hexagonal polytypes with Co^{III} in face-shared octahedra, as in 12H-$BaCo_{0.6}Mn_{0.4}O_{2.83}$ or 12H-$BaCoO_{2.6}$, Co^{III} adopts a high spin electronic configuration (4.9 μ_B). In addition, it has recently been reported that an intermediate spin-state for Co^{IV} in $Ba_5Co_5FO_{13-\delta}$[36] may result from crystal field splitting arising from a distorted tetrahedral environment. If an intermediate spin state configuration is therefore assumed for Co^{IV} (3.87 μ_B) and a high spin state for Co^{III} in the octahedral sites (4.9 μ_B) an effective moment of 4.31 μ_B/metal ion is obtained which is also in good agreement with the experimental value. Because a subtle deviation from a pure Curie–Weiss behavior is observed from 150 K down to the Curie–Weiss temperature, indicating the existence of short-range magnetic correlations in this material, the experimental value obtained from the Curie-Wiess fit rendering a paramagnetic moment of 3.7 μ_B/metal ion does not allow discrimination between the two proposed models.

To assess the existence of spin disorder in $BaMn_{0.2}Co_{0.8}O_{2.80}$, ZF ac magnetic susceptibility with an ac field of 10 Oe was performed over a wide frequency range, Figure 7. A clear peak is detected at $T \approx 35$ K in both the real, χ', and imaginary, χ'', components of the magnetic susceptibility. This temperature coincides with the high temperature transition defined by the first derivative of the dc-susceptibility. Interestingly, the peaks in χ' and χ'' shift to higher temperature with increasing frequency as expected for a spin glass system. ac magnetic susceptibility measurements were performed under several applied dc fields (1–50 kOe), Figure 8. The temperature associated with the peak maximum in χ' does not exhibit a strong dependence on the application of modest dc fields, as is observed in many spin glasses. In contrast, at high dc fields the peak seems to shift toward higher temperatures, as is expected for a ferromagnet. Note

(33) Leslie-Pelecky, D. L.; Rieke R.D, *Chem. Mater.* **1996**, *8*, 1770.
(34) Jin, R.; Sha, H.; Khalifah, P. G.; Sykora, R. E.; Sales, B. C.; Mandrus D., Zhang J, *Phys. Rev. B* **2006**, *73*, 174404.
(35) Boulahya, K.; Parras, M.; Gonzalez-Calbet, J. M.; Amador, U.; Martinez, J. L.; Fernandez-Diaz M.T, *Chem. Mater.* **2006**, *18*, 3898.
(36) Ehora, G.; Renard, C.; Daviero-Minaud, S.; Mentré O, *Chem. Mater.* **2007**, *19*, 2924.

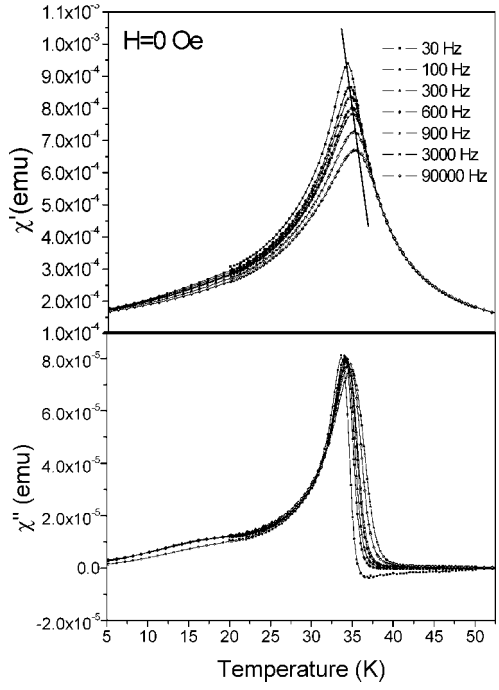

Figure 7. χ' and χ'' versus temperature for $BaMn_{0.2}Co_{0.8}O_{2.80}$.

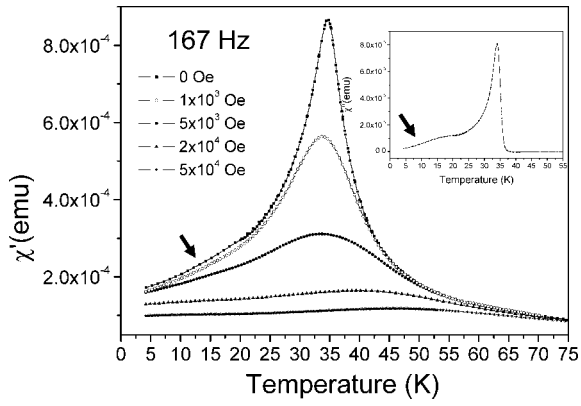

Figure 8. χ' versus temperature as a function of dc magnetic field for $BaMn_{0.2}Co_{0.8}O_{2.80}$. Inset shows χ'' versus temperature.

also that a small and broad anomaly appears around 20 K, coinciding with the onset of the irreversible behavior in the ZFC-FC data shown in Figure 7. This anomaly becomes more obvious in the plot of losses, shown in the inset, and is reminiscent of that observed for the neighboring compound $BaCo_{0.6}Mn_{0.4}O_{2.83}$.

To further explore the origin of the behavior of the ZFC and FC data, magnetization versus magnetic field ($M-H$) data were collected at several temperatures. Above 60 K, the data present ideal linear paramagnetic behavior, Figure 9 a; however, below this temperature, the system exhibits the behavior of a superparamagnet that remains unblocked down to 40 K. At 35 K, the $M-H$ data exhibit hysteresis with a nonzero remanence and a nonzero coercivity, as in a conventional ferromagnet. At the lowest temperature (2 K), a dramatic enhancement of the coercivity occurs, although saturation is not observed, even at 50 kOe, Figure 9c. At this temperature, the M-H data closely resemble what it is expected for an assembly of non interacting, single domain, ferromagnetic uniaxial particles having their axes randomly oriented, as described by the Stoner–Wohlfarth model.[37]

The magnetism of $BaMn_{0.2}Co_{0.8}O_{2.8}$ at low temperatures (<150 K) is clearly rather complex; however, the overall picture that emerges from the low temperature data is that of a system composed by some kind of ferromagmagnetic clusters, associated with crystallographic domains, small enough to show superparamagnetic behavior above 30 K. Below this temperature the magnetization of these entities blocks and they become aligned along the easy magnetization axis in a random orientation. These ferromagnetic clusters are assigned to groups of Co atoms that occupy neighboring positions, either on octahedral or tetrahedral sites between Mn atoms located only on octahedral positions in the structure. Because of the randomness introduced by the presence of the Mn atoms, the easy axis of the Co clusters is randomly oriented and, additionally, a rather narrow distribution of cluster sizes is expected. Also, the ferromagnetic character of the Co clusters is consistent with the observation of ferromagnetic interactions between Co^{4+}-Co^{4+} (tetrahedral coordination) and Co^{3+}-Co^{3+} (in octahedral coordination) in closely related compounds such as Ba_2CoO_4[34,35] and 5H-$BaCoO_{2.8}$.[23]

The described scenario of a random-anisotropic system has obvious consequences for the magnetic properties. First, long-range magnetic order is precluded in the presence of random magnetic anisotropy, according with general theoretical results,[38] and second, strong magnetic hardening is expected at low temperatures in the Stoner–Wohlfarth model.[37] This enhancement of the coercivity can be understood in terms of the two basic mechanisms leading to magnetic moment reversal: domain wall motion and coherent rotation of the spins. The latter requires a larger external field energy to occur as compared with that of the former. In large particles or clusters, where there are many magnetic domains, the coercivity is mainly determined by domain wall motion but as the cluster size decreases to a few lattice spacings, as it is in this case, the formation of domain walls is energetically unfavorable and the clusters become monodomains. Changes in the magnetic moment can then occur only through coherent rotation of the spins, and a giant intrinsic magnetic hardness is predicted that translates into an enhancement of the coercivity, as is observed at low temperatures.

In summary, a Stoner–Wohlfarth model of random-anisotropic, non-interacting monodomain ferromagnetic clusters seems in order to describe the magnetic behavior of $BaMn_{0.2}Co_{0.8}O_{2.80}$. In this system, it is the randomness in anisotropy introduced by the Mn ions which prevents the transition into long-range three-dimensional ferromagnetic order achieved in the parent compound $BaCoO_{2.8}$[23] at ~47 K.

Electrical Properties. Impedance Spectroscopy and fixed frequency capacitance and dielectric loss measurements were performed on ceramics (~ 70% of the theoretical density) of $BaMn_{0.2}Co_{0.8}O_{2.8}$. Room-temperature measurements showed

(37) *Introduction to Magnetic Materials*; Cullity, D., Ed.; Addison-Wesley: Sebastopol, CA, 1972; pp 362–367.
(38) Pelcovits, R. A. *Phys. Rev.* **1979**, *19*, 465.

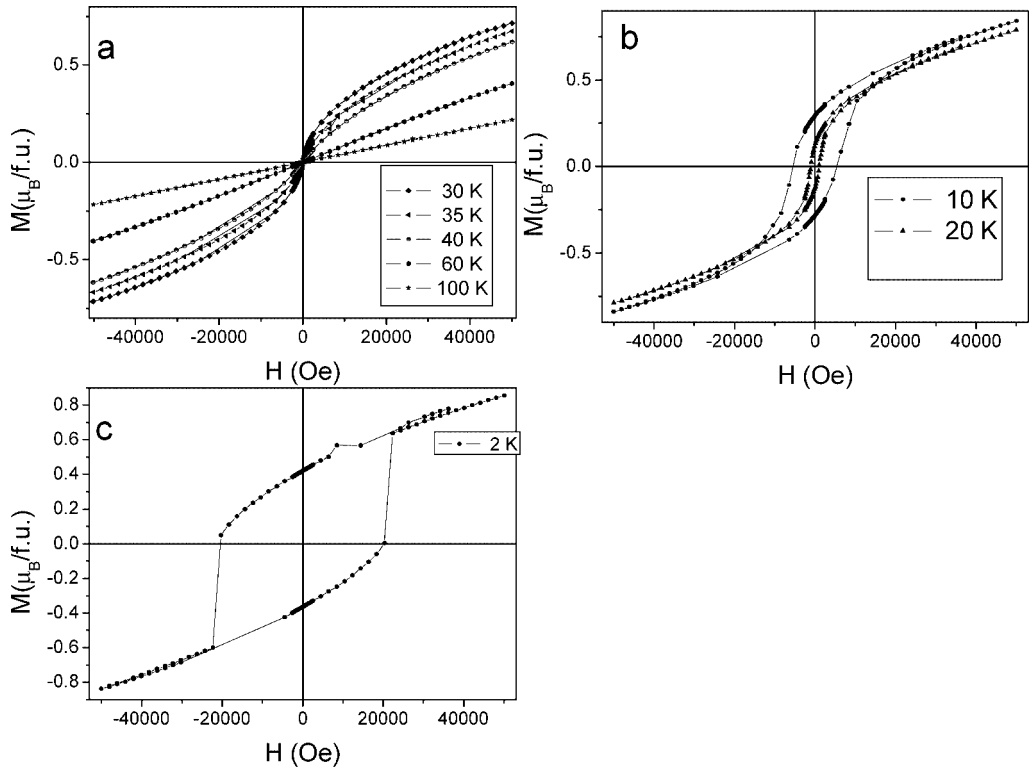

Figure 9. M versus H for $BaMn_{0.2}Co_{0.8}O_{2.80}$ at (a) 30–100 K, (b) 10 and 20 K, and (c) 2 K.

the ceramics to be semiconducting (<100 Ωcm) and therefore subambient measurements were required to obtain meaningful data. An impedance complex plane, Z*, plot is shown for a temperature of 60 K, Figure 10 a, and reveals the presence of two semicircular arcs. The total resistivity, R_T, of the ceramic is ∼0.37 MΩcm and based on an equivalent circuit consisting of two parallel resistance−capacitance (RC) element connected in series to model the data (to a first approximation) the C values associated with the low and high frequency arcs are ∼4 $nFcm^{-1}$ and ∼2 $pFcm^{-1}$, respectively. On the basis of the brickwork model for electroceramics these values are consistent with responses expected for grain boundary and bulk (grain) components, respectively. The total resistivity of ∼0.37 MΩcm at 60 K can therefore be subdivided into a combination of bulk, R_b ≈ 0.22 MΩ cm, and grain boundary, R_{gb} ≈ 0.15 MΩ cm, contributions.

An Arrhenius plot of bulk and grain boundary conductivity (where $\sigma = 1/R$) data extracted from the intercepts of the two arcs on the real axis of the Z* plots is shown in Figure 10 b and reveals two interesting features. First, σ_b does not obey the Arrhenius law, instead there appears to be a gradual change from thermally activated conductivity behavior with an activation energy, E_a, of ∼0.07 eV in the range ∼70–130 K to a low temperature state (<20 K) where E_a associated with the bulk conductivity is extremely low, < 3 meV.

Attempts to fit the bulk conductivity data to other conduction type models, eg variable range hopping (VRH) were also unsuccessful. For example, the variation in bulk resistivity with temperature to $T^{-1/x}$ ($1 \leq x \leq 4$) is shown in Figure 10 c and all show distinct curvature, especially at low temperatures. The standard Mott $T^{-1/4}$ plot is a better fit than the Arrhenius T^{-1} plot; however, no value of x gives a linear fit over the measured temperature range. It is interesting to note that similar resistivity behavior has been reported for the 2H perovskite $Ba_{0.8}La_{0.2}CoO_3$,[39,40] which can be considered structurally (and possibly electrically) as a 1D compound because of its 2H hexagonal structure formed by 1D chains of face sharing CoO_6 octahedra that are separated by Ba/La atoms. Although 5H-$BaMn_{0.2}Co_{0.8}O_{2.8}$ cannot be described structurally as a 1D compound there is clear anisotropy in the crystal structure and the two compounds may have similar conduction mechanisms. At present, an explanation for the type of conduction observed for 2H-$BaCoO_3$ and for 5H-$BaMn_{0.2}Co_{0.8}O_{2.8}$, Figure 10 c, is not clear; however, for the compound studied here it may be associated with Anderson localization, anisotropic conduction associated with the 5H perovskite-type cell or some complex correlated mechanism between the magnetic and electronic transport properties.

Closer inspection of the IS data at low temperature, e.g., 22 K, reveals the high frequency arc associated with the bulk response to be extremely nonideal, Figure 10 d and a combined plot of the imaginary components of impedance and electric modulus further highlight the nonideal Debye-like response of the bulk component, Figure 10 e. For example, the half-height peak width of the Debye peak in both spectra far exceeds the ideal value of 1.14 decades (on a log f scale) and the relaxation frequency of the two peaks is not coincident; instead they differ by more than one decade. This nonideal behavior may arise due to some of the factors mentioned above, alternatively it may be associated with the grains being electrically heterogeneous. This

(39) Yamaura, K.; Cava, R. J. *Solid Sate Commun.* **2000**, *115*, 301.
(40) Yamaura, K.; Zandbergen, H. W.; Abe, K.; Cava, R. J. *J. Solid State Chem.* **1999**, *146*, 96.

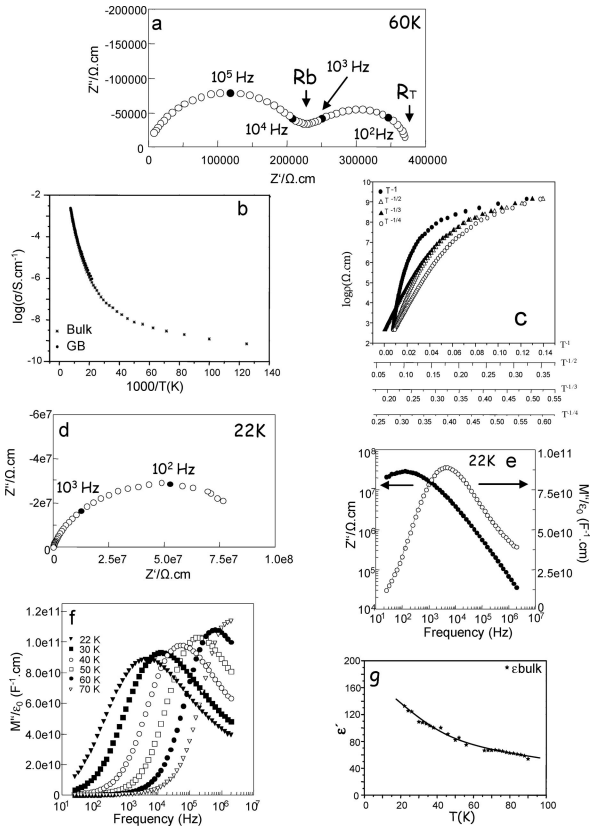

Figure 10. Summary of impedance spectroscopy data for $BaMn_{0.2}Co_{0.8}O_{2.8}$ ceramics. (a) Z* plot at 60 K; (b) Arrhenius plot of bulk and grain boundary conductivity data; (c) log (bulk resistivity) versus $T^{-1/x}$ for $x = 1-4$; (d) Z* plot at 22 K; (e) Z″ and M″ spectroscopic plots at 22 K; (f) M″ spectroscopic plots at selected temperatures; and, (g) bulk permittivity versus temperature.

heterogeneity may arise due to the development of oxygen concentration gradients within the grains during and after the sintering process that is required to make ceramics for IS measurements. This is often the case when preparing mixed metal oxides that contain transition metal cations such as Co and/or Mn that can exhibit variable oxidation states when heat treated in air at elevated temperatures. Electrical property measurements are very sensitive to low levels of oxygen nonstoichiometry in transition metal oxides and further studies are required to investigate the influence of sintering conditions on the electrical properties of 5H-$BaMn_{0.2}Co_{0.8}O_{2.8}$.

Spectroscopic plots of the imaginary component of the electric modulus, M″, are a useful representation of IS data to study any temperature variation of the bulk permittivity. M″ spectra for 5H-$BaMn_{0.2}Co_{0.8}O_{2.8}$ show a systematic increase in peak height with temperature, Figure 10 f, and due to the inverse relationship between M″ and permittivity, the bulk permittivity decreases with increasing temperature, Figure 10 g. The magnitude of the permittivity (∼50–150) is higher than expected from a Clausius Mossotti calculation based on molar volume and ion polarisibilities, however, this may be due to a combination of electrical heterogeneity, the rather leaky nature of the grains and/or errors associated with data extraction using nonideal M″ Debye peaks. Nevertheless, the data reveal the permittivity to decrease smoothly with increasing temperature and that no dielectric anomaly occurs at the onset/break-up of the ferromagnetic clusters at ∼ 35 K, Figure 9.

5H-$BaMn_{0.2}Co_{0.8}O_{2.8}$ ceramics are electrically heterogeneous as shown by the presence of two arcs in the Z* plot at 60 K, Figure 10 a. The low frequency arc was attributed to a grain boundary component due to the magnitude of the capacitance (∼nFcm^{-1}) associated with the arc. It is noteworthy that polishing the major pellet faces and remeasuring the ceramics did not produce any change to the impedance spectroscopy data. This confirms the low frequency arc in the Z* plots to be associated with a grain boundary component as opposed to a surface layer on as-sintered ceramics. Different types of grain boundaries can form in ceramics and in the present case the grain boundary response is attributed to a so-called "constriction resistance" that is associated with "necking" between grains within the ceramics. Justification for this is two-fold. First, the grain boundary (GB) conductivity shows similar behavior to the bulk conductivity, Figure 10 b, and second, the low density (70%) of the pellet. Incomplete or partial sintering of ceramics often results in the development of necking between grains as opposed to the development of well-defined, grain boundary regions. In this case, the grain boundary regions consist of the same bulk phase and therefore have similar conductivity behavior but have a lower volume fraction due to the presence of porosity and therefore have higher associated capacitance.

The electrical microstructure of 5H $BaMn_{0.2}Co_{0.8}O_{2.8}$ ceramics consists of semiconducting grains and constrictive grain boundaries and should therefore give rise to an Internal Barrier Layer Capacitance (IBLC) effect. Fixed frequency capacitance and dielectric loss measurements were performed and the results confirm IBLC behavior, Figure 11. The low permittivity plateau (<100) at low temperature is associated with the grain response and the large increase in permittivity and high permittivity plateau (∼10 000) at high temperature is associated with the constrictive grain boundary response, Figure 11 a. tan δ values are high (>2) and the data show the presence of a peak that occurs at higher temperature with increasing frequency. The origin of this peak is due to a parasitic series capacitance effect associated with the series combination of R_b and C_{gb} elements in the equivalent circuit. The IBLC effect in this compound is unlikely to find commercial applications due to the high tan δ. Chemical doping to reduce the bulk resistivity by at least 2 orders of magnitude and improvements in the ceramic processing to increase the grain boundary resistivity by at least 2 orders of magnitude are required before this compound could be considered as a viable IBLC.

In conclusion, the 5H-type hexagonal structure of $BaMn_{0.2}Co_{0.8}O_{2.8}$ has been established and is isostructural with that of 5H-$BaCoO_{2.8}$. Twenty % replacement of Co by Mn(+IV) on the face sharing octahedral sites has a dramatic effect on the magnetic properties with ferromagnetic ordering at ∼47 K being replaced by magnetic behavior best described by a Stoner–Wohlfarth model of random-anisotropic, non-interacting monodomain ferromagnetic clusters. $BaMn_{0.2}Co_{0.8}O_{2.8}$ also exhibits complex semiconducting electrical

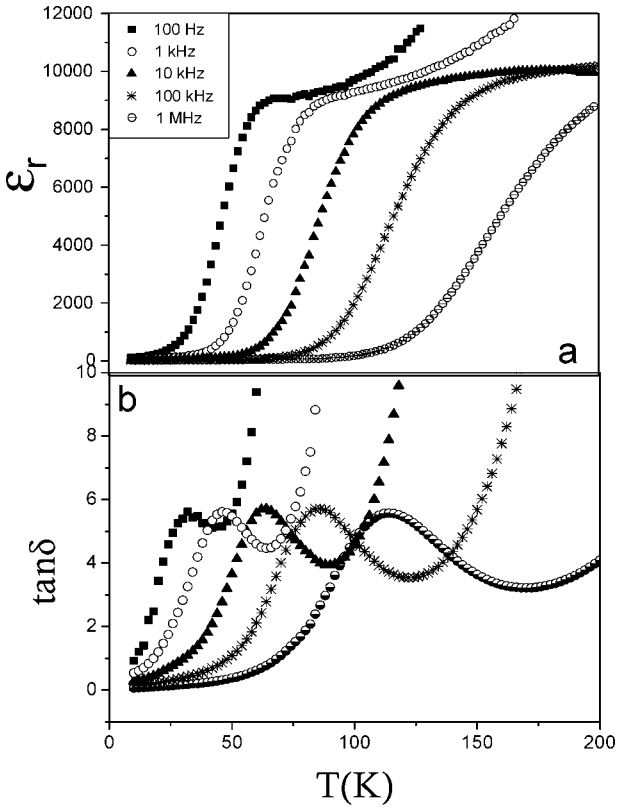

Figure 11. Fixed frequency (a) permittivity and (b) tan δ versus temperature for $BaMn_{0.2}Co_{0.8}O_{2.80}$ ceramics.

behavior at subambient temperatures. This behavior is inconsistent with conventional conduction models such as the Arrhenius law or Variable Range Hopping and is qualitatively similar to that observed for 2H-$Ba_{0.8}La_{0.2}$-CoO_3.[39] Several suggestions have been made to explain the conductivity behavior; however, further studies on $BaMn_{0.2}Co_{0.8}O_{2.8}$ and related hexagonal-type cobaltites are now required to establish if this conduction behavior is common to all these materials and to establish its origin(s). $BaMn_{0.2}Co_{0.8}O_{2.8}$ ceramics are electrically heterogeneous and consist of semiconducting grains and constrictive grain boundaries. Such an electrical microstructure gives rise to very high apparent permittivity values from fixed frequency capacitance measurements, e.g., ~10 000 at 10 kHz for >100 K; however, impedance spectroscopy data reveals the bulk permittivity to be ~50 at 100 K. The high apparent permittivity is therefore attributed to an extrinsic IBLC mechanism associated with the constrictive grain boundaries as opposed to an intrinsic value associated with the crystal structure.

It is also noteworthy that in all oxygen-deficient hexagonal cobaltites reported to date that the presence of anion vacancies appears to stabilize a cc'c structural unit (where c′ refers to a cubic BaO_2 layer) within the crystal structure and this results in the formation of a double tetrahedral layer. Such tetrahedral oxygen coordination is likely for Co(+IV) and this seems to have a "structure-directing" effect on the stacking sequences adopted by hexagonal-type, anion-deficient cobaltites. This is in contrast to that reported for oxygen-deficient manganates[9] and titanates,[41] where anion vacancies are located in h- rather than c-stacked layers.

Acknowledgment. Financial support through research project MAT2004-01248 (Spain), FAME-EU (Madrid, Sheffield), EPSRC (PP-grant, Sheffield), and EU (NUOTO, Sheffield) is acknowledged. We thank Dra. M.T. Fernández-Díaz for assistance in collecting the neutron powder diffraction data.

CM703447W

(41) Sinclair, D. C.; Skakle, J. M. S.; Morrison, F. D.; Smith, R. I.; Beales T.P, *J. Mater. Chem.* **1999**, *9*, 1327.